ChemPhotoChem

Chemistry Europe
European Chemical Societies Publishing
ChemPhotoChem

RESEARCH ARTICLE

Bis-Diimine Rhenium(I) Complexes for Biomedical Photoacoustic Tomography

Svetlana G. Madieva[1] | Kristina S. Kisel[1] | Julia R. Shakirova[1] | Elizaveta V. Durova[1] | Sergey A. Silonov[1,2] | Vitaly V. Porsev[1] | Robert A. Evarestov[1] | Pavel V. Subochev[3] | Alexey A. Kurnikov[3] | Anna G. Orlova[3] | Ilya V. Turchin[3] | Tzu-Ming Liu[4] | Sergey P. Tunik[1]

[1]Institute of Chemistry, St Petersburg University, St. Petersburg, Russia | [2]Department of Cytology, Russian Academy of Sciences, St. Petersburg, Russia | [3]Department of Radiophysical Methods in Medicine, Federal Research Center A.V. Gaponov-Grekhov Institute of Applied Physics of the Russian Academy of Sciences, Nizhny Novgorod, Russia | [4]Ministry of Education, Frontiers Science Center for Precision Oncology, University of Macau, Macau, China

Correspondence: Sergey P. Tunik (sergey.tunik@spbu.ru)

Received: 9 September 2025 | **Revised:** 12 November 2025 | **Accepted:** 1 December 2025

Keywords: biocompatibility | bis-diimine rhenium(I) complexes | near-infrared absorption | photoacoustic imaging

ABSTRACT

A series of bis-diimine rhenium(I) complexes **Re(NN1-OMe)–Re(NN3-OMe)**, containing neocuproine and methyl [2-(pyridin-2-yl)quinoline-4-carboxylate (NN1), methyl [2,2′-biquinoline]-4-carboxylate (NN2), dimethyl [2,2′-biquinoline]–4,4′-dicarboxylate (NN3) was synthesized and characterized. Utilization of the asymmetric NN1 and NN2 ligands affords two types of structural isomers, which were isolated and structurally studied by X-ray diffraction analysis in the solid state. ^{1}H-^{1}H COSY and NOESY NMR experiments confirmed preservation of the structural patterns in liquid media for the complexes under study. Alkaline hydrolysis of the ester groups in the NN# diimine ligands was performed to give the **Re(NN1-OK)–Re(NN3-OK)** complexes exhibiting higher water solubility that made possible to use them in biological experiments. In MeOH and aqueous media, the complexes display NIR absorption with a long wavelength band at ca. 715 nm extended up to 850 nm in the case of both forms of **Re(NN3)-OX**. The **Re(NN3-OK)** complex demonstrated stable photoacoustic signal in oxygenated blood phantoms and showed no significant toxicity with the cell viability above 80% even at concentrations of 1 mM in cell experiments with CHO-K1 cell line.

1 | Introduction

Photoacoustic or optoacoustic imaging is a hybrid modality, combining the high molecular specificity of optical imaging with the superior spatial resolution and penetration depth of ultrasound for various biomedical applications [1]. Endogenous (intrinsic) chromophores like hemoglobin, water and melanin provide natural contrast for PAI, however, they show considerable tissue background noise, limited visualization depth, and restricted imaging site selection [2]. The development of exogenous contrast agents has become crucial for expanding the technique's applications, allowing for greater detection sensitivity particularly in the transparent near-infrared (NIR) window (700–1700 nm), and enabling conjugation with targeting molecules [3].

Current NIR photoacoustic contrast agents can be broadly categorized into several classes: small organic molecules, inorganic nanoparticles, organic nanoparticles and emerging molecular complexes [4]. Small organic dyes, such as indocyanine green (ICG)—the first FDA-approved NIR contrast agent [5] are biocompatible and easily eliminated from the body, but these chromophores obviously suffer from rapid photobleaching, nonspecific binding, uncontrolled aggregation, and limited ability for functionalization/vectorization [6]. On the contrary, gold-based nanostructures including nanorods and nanoshells offer enhanced photostability and surface plasmon resonance tuning [7] whereas carbon nanotubes and other carbon-based nanomaterials demonstrate exceptional NIR absorption and can be used as a theranostic platform [8]. However, these inorganic nanoparticles face challenges with potential toxicity concerns, damage to the cardiovascular and respiratory systems, and inflammatory responses [9, 10].

Recent advances have focused on metal-based complexes as a promising alternative to nanoparticles, enhancing permeability in tissue and clearance from the body. Due to their molecular

nature, these compounds could be easily modified towards the development of agents with tailored photophysical and pharmacological properties [11]. However, metal-based complexes suffers from low light absorption in NIR, and only a few studies reported on some progress aimed at overcoming of this problem for their applications in deep PAI [12].

The development of "smart" photoacoustic probes that can simultaneously provide anatomical contrast and report on local biochemical conditions (e.g., pH, enzyme activity, or redox status) represents a particularly urgent need in the field [13, 14]. For instance, tumor microenvironments are characterized by acidic extracellular pH (6.5–7.0) compared to normal tissues (7.2–7.4) [15], generating a demand for pH-responsive contrast agents that could improve tumor delineation [16].

In this context, we report on the design and synthesis of a series of novel water-soluble rhenium(I) complexes that addresses these critical needs. It was shown that rational design of ligand environment allows for obtaining the complexes (**Re(NN3-#)**) that exhibits: (1) strong NIR absorption centered at 715 nm, (2) excellent aqueous solubility (>10 mM) without requiring formulation aids, (3) a very low toxicity in preliminary cell studies ($CC_{50} > 1000$ μM), and (4) modular ligand architecture, which enables a straightforward conversion into environment-sensing chromophores, as demonstrated by their pH-responsive PA behavior. It is obvious that photoacoustic imaging (PAI) contrast agents require substantial light absorption in the NIR region. Carbonyl complexes of rhenium(I) with diimine ligands typically demonstrate $S_0 \rightarrow S_1$ absorption of the ^{1}MLCT type, the energy of which could be tuned by modification of coordinated diimine, e.g. by expansion of aromatic system and insertion of electron-withdrawing substituents into the diimines. In our previous publication [17], we showed that the mixed-ligand bis-diimine rhenium(I) complexes with the ligands containing quinoline fragment display absorption in the region of ca. 600–700 nm. In the current study we used the ligands containing quinoline moiety with electron-withdrawing ester group: methyl 2-(pyridin-2-yl) quinoline-4-carboxylate (NN1), methyl [2,2′-biquinoline]-4-carboxylate (NN2), dimethyl [2,2′-biquinoline]−4,4′-dicarboxylate (NN3), to synthesize the rhenium(I) complexes. It is also important to note that the ester group can be easily hydrolyzed to carboxyl group, which can improve the solubility of the complexes in water, as this is one of the major requirements for practical applications in biological systems. Cellular experiments with Chinese hamster ovary (CHO-K1) cells also demonstrated the biocompatibility of the hydrolyzed **Re(NN3-OK)** complex. Through comprehensive phantom studies, it was shown that this complex displays significantly enhanced photoacoustic contrast compared to endogenous absorbers while maintaining excellent stability. The obtained results establish the Re(I) complexes as a promising platform for developing multifunctional photoacoustic agents that combine imaging performance with sensing capabilities.

2 | Results and Discussion

2.1 | Synthesis and Characterization

The **Re(NN#-OMe)** complexes were synthesized according to the published procedure [17], see Scheme 1. The use of the asymmetric NN1 and NN2 ligands made possible isolation of two types of structural isomers for the complexes containing these ligands. The isomers where the methylquinoline-4-carboxylate fragment is in *trans* position to a carbonyl ligand are denoted "a", and the isomers with the same fragment in *cis* position to the both carbonyl ligands are denoted "b" (Scheme 1). The overall yields of the reactions are quite high, but the ratio of a/b isomers varies depending on the ligand. In the case of NN1 the main product is isomer "a" (yield 70%), while for NN2 the yields of both isomers are almost equal. We suggest that one of the driving forces in formation of the final compound is intramolecular $\pi\cdots\pi$ interaction [18] of incoming diimine with neocuproine ligand that has been illustrated by solid state structural data, vide infra. From this point of view, the variations in the ratio of obtained isomers can be explained by the difference in the properties of the aromatic system of the second diimine. Indeed, for the complexes with the NN1 ligand, the "a" isomer dominates because the larger methylquinoline-4-carboxylate moiety interacts more effectively with the aromatic system of neocuproine compared to smaller pyridine fragment, while in the case of NN2 the quinoline and methylquinoline-4-carboxylate moieties are almost equivalent in this respect.

The hydrolyzed **Re(NN#-OK)** complexes were prepared by heating the parent compounds in methanol solution in the presence of potassium carbonate at 40°C for 12 h. In the case of **a/b-Re(NN1-OMe)** complexes, we isolated the corresponding **a/b-Re(NN1-OK)** isomers in good yields, while in the case of **a/b-Re(NN2-OMe)**, the hydrolysis gave a mixture of isomers regardless of which isomer "a" or "b" was used as the starting compound. This behavior indicate that free energies of the **a/b-Re(NN2-OK)** isomers are close each other and the isomerization energy barrier is relatively low.

Solid state structures of the **a/b-Re(NN1-OMe)** isomers were determined by X-ray diffraction (XRD) analysis (Figure 1, Tables S1 and S2, Figures S1 and S2). According to the data obtained the rhenium centers adopt distorted octahedral geometry due to the presence of intramolecular $\pi\cdots\pi$ interaction between the aromatic systems of coordinated diimine ligands. In both cases two optical isomers present in the solid state (Figure S1). In the case of **b-Re(NN1-OMe)**, only one (pyridine) ring is involved in π-stacking, whereas in **a-Re(NN1-OMe)** both condensed rings of the methylquinoline-4-carboxylate fragment are involved in the interaction. The distances between centroids of the interacting aromatic rings in the isomers are within 3.9–4.0 Å, which indicate strong interaction [19]. The bond lengths and angles in the studied complexes (Table S2) fall in the ranges characteristic of (bis)diimine rhenium carbonyl compounds [17, 20]. The packing of the molecules in crystal cells is dictated by various short interatomic contacts including intermolecular $\pi\cdots\pi$, C–H···O≡C(carbonyl), C–H···O=C(ester) and C–H···C(aromatic) interactions (Figure S2).

In solution, the obtained complexes were fully characterized by ^{1}H, ^{1}H–^{1}H COSY, ^{1}H–^{1}H NOESY NMR spectroscopy (Figures S3–S19), ESI^+ mass spectrometry (Figures S20) and IR spectroscopy (Figures S21 and S22). The relative intensities, chemical shifts and multiplicities of the signals in the proton NMR spectra are in complete agreement with the molecular structures represented in Scheme 1 and found in the solid state (Figures S3–S12). The complete assignment of the signals in the proton spectra was made on the basis of ^{1}H-^{1}H COSY and ^{1}H-^{1}H NOESY data. The signals of the neocuproine ligand appear as three sets of doublet pairs in the aromatic region and as two singlets from methyl groups in the aliphatic region. In all cases, one of the methyl groups is

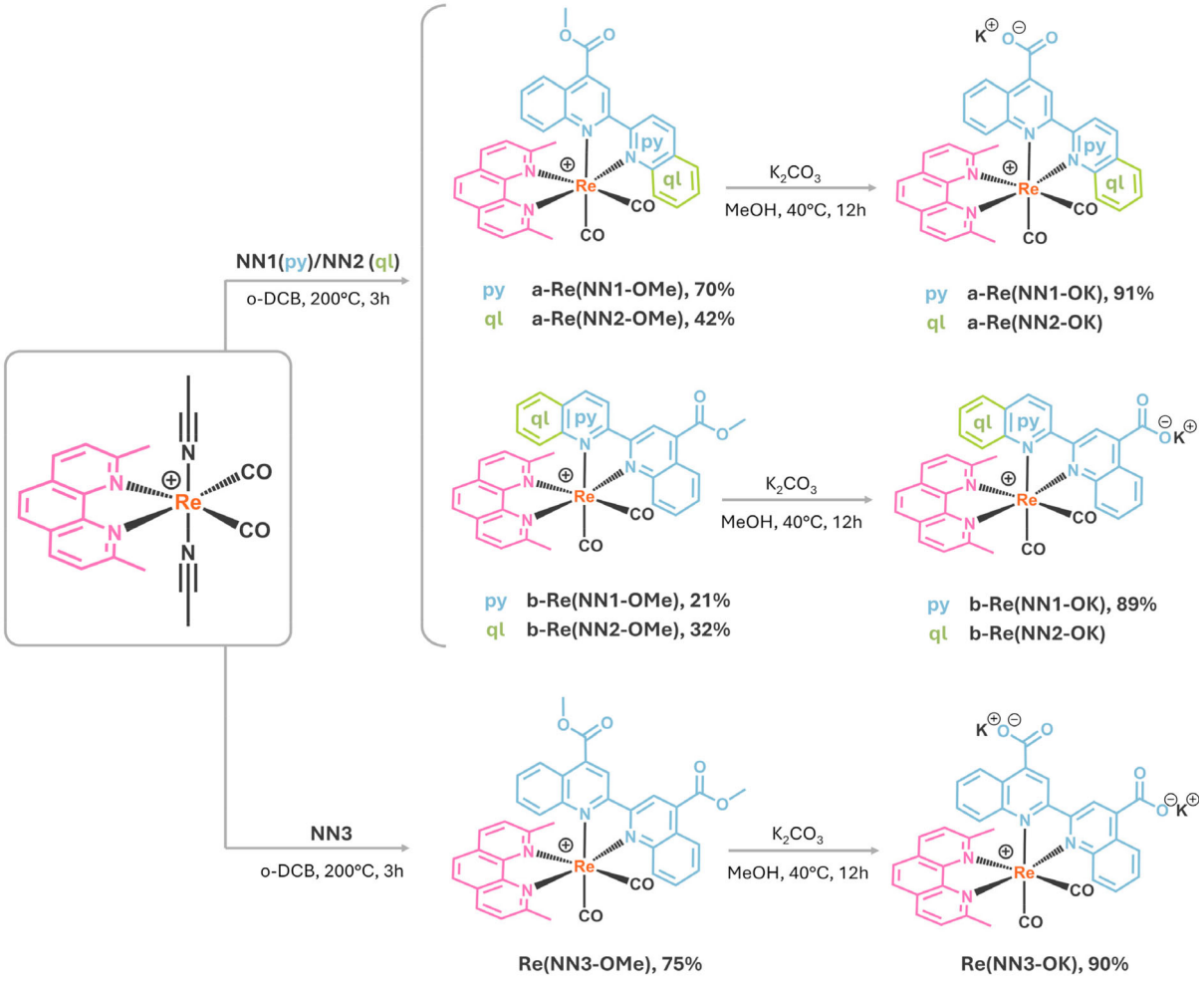

SCHEME 1 | Synthesis of bis-diimine rhenium(I) complexes.

significantly high field shifted due to the influence of the aromatic ring currents of another diimine ligand [21–25], as the methyl substituent is involved in the interaction with this aromatic system (Figure 1, Figures S3–S12). The chemical shifts of the other protons strongly depend on the mutual orientation of the diimine ligands in the complex, which is well illustrated by comparing XRD data and NMR spectra of two structural isomers of the **Re(NN1-OMe)** complex (Figure 1). In both cases, the most shielded protons in the aromatic region belong to the NN1 ligand fragment involved in π-stacking with neocuproine: methylquinoline-4-carboxylate in the case of **a-Re(NN1-OMe)** or pyridine in the case of **b-Re(NN1-OMe)**. The cross-peaks between the protons of neocuproine and NN# ligands in the ^{1}H-^{1}H NOESY spectra correlate well with the distances of shorter than 3 Å between them found in the corresponding solid-state structures, see Figure 1.

Upon hydrolysis, the signals related to the ester group disappear confirming the formation of carboxyl functions. The other observed signals indicate that the main structural motifs found in the parent compounds remain unchanged (Figures S13–S18). Only in the case of **a/b-Re(NN2-OMe)** complexes, a mixture of both isomers appears in the NMR spectra after hydrolysis (Figure S19), vide supra. The ESI^{+} mass spectra of **Re(NN#-OMe)** complexes and their hydrolyzed forms **Re(NN#-OK)** fit well the stoichiometry of the obtained compounds (Figure S20). FTIR spectra of **Re(NN#-OMe)** and **Re(NN#-OK)** show two absorption bands, corresponding to the symmetric (ca. 1838–1852 cm^{-1}) and asymmetric (ca. 1914–1921 cm^{-1}) C≡O stretching vibrations typical for the bis(carbonyl) rhenium(I) complexes (Figures S21 and S22) [17, 26–28]. In summary, the above mentioned spectral data indicate that in solution the complexes retain the structural patterns found in solid state.

Absorption spectra of the **Re(NN#-OMe)** and **Re(NN#-OK)** complexes were measured in methanol, see Figures 2 and S23, S24, numerical data are compiled in Table 1. Because of appreciable water-solubility of **Re(NN3-OK)**, its absorption spectra were also recorded in aqueous solution (Figure 3).

The **Re(NN#-OMe)** complexes show absorption in almost the whole visible region of the spectrum. The long-wavelength tails extend up to 800–900 nm. According to the literature data the high-energy absorption bands (250–300 nm) could be assigne to the ^{1}LC transitions in the aromatic systems of diimine ligands [20, 26–28]. Bands in the 300–550 nm interval could be attributed to the mixed ^{1}MLCT/^{1}LLCT/^{1}ILCT transitions [20, 26–28], whereas the low-energy bands in the region below 550 nm were assigned to the ^{1}MLCT transitions, d(Re) → π^*(NN) [20, 26–28]. Variations in the nature of the diimine ligand results in a systematic red shift of the low energy absorption in the series pyridine (NN1) → quinoline (NN2) → methylquinoline-4-carboxylate (NN3) (Figure 2). This effect correlates with the lowering the energy of π^*(NN) orbitals upon expansion of the aromatic system or

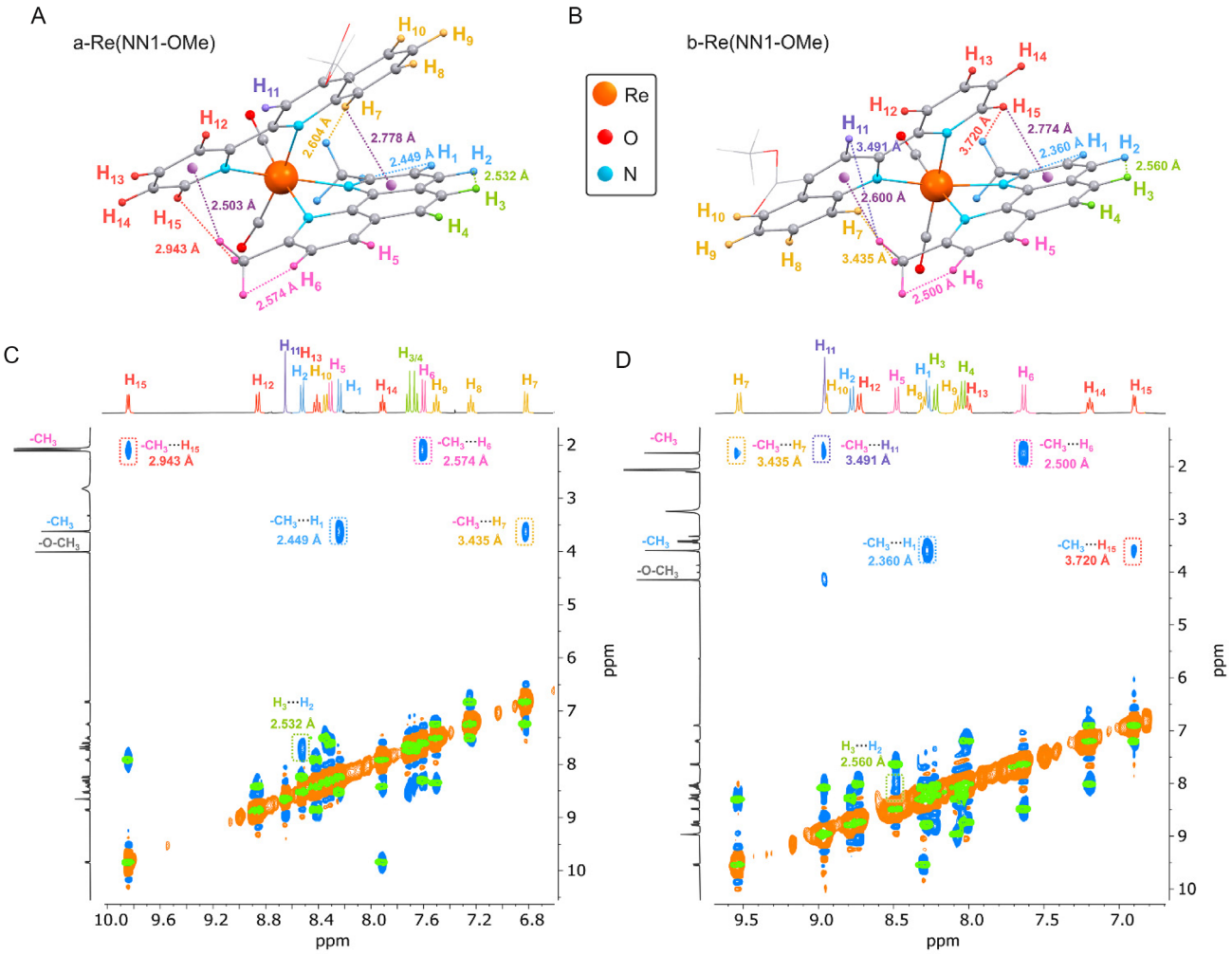

FIGURE 1 | Molecular views of **a-Re(NN1-OMe)** (A) and **b-Re(NN1-OMe)** (B), showing selected short intramolecular contacts. Overlay of ^{1}H-^{1}H COSY (green color) and NOESY (orange color–exchange peaks; blue color–through space interactions) of **a-Re(NN1-OMe)** (C) and **b-Re(NN1-OMe)** (D) in acetone-d_6 at 298 K, 400 MHz.

introduction of an electron-withdrawing substituent [27, 29], the absorption of the "a" isomer being slightly red shifted compared to that of the "b" isomer (Figure 2B).

Upon hydrolysis the ester groups of the complexes are transformed to the carboxylic functions that may exist in two forms depending on pH: deprotonated (**Re(NN#-OK)**) or the protonated one (**Re(NN#-OH)**). Under acidic conditions, the **Re(NN#-OH)** complexes exhibit absorption spectra closely resembling those of their parent ester compounds (Figure 3 and S23), whereas under basic conditions, a hypsochromic shift of the lowest energy band is observed. According to TD-DFT calculations, the nature of S_0-S_1 transitions in protonated and deprotonated forms is almost the same (Table S3, Figures S25–S32), which allows concluding that the observed hypsochromic shift is related to the variations in the electronic properties of the –C(O)OX substituents from an electron-acceptor –C(O)OH to a weak electron-donor –C(O)OK [30, 31].

Among the studied **Re(NN#-OK)** complexes **Re(NN3-OK)** demonstrates the best water-solubility and absorption in the region suitable for the photoacoustic experiments. Therefore we studied the dependence of **Re(NN3-OK)** absorption on pH and calculated pKa, which was found to be approximately 2.9 (Figure S24). Unfortunately, this pKa value is outside the region of biological importance (pH 5–8) that prevents the complex application as a pH sensor in biological studies. Nevertheless, **Re(NN3-OK)** is an excellent candidate for potential use as contrast agent. Additionally, to assess the potential applicability of **Re(NN3-OK)** in photoacoustic experiments, its photostability under irradiation was studied (Experimental Section). The methanol solution of **Re(NN3-OK)** was irradiated with UV lamp and the absorption and ^{1}H NMR spectra were measured. The absence of spectral differences between the fresh methanol solution of **Re(NN3-OK)** before irradiation and the irradiated **Re(NN3-OK)** solutions revealed the stability of the named complex under photoexcitation (Figure S34).

2.2 | Photoacoustic Phantom Studies and MTT Assay

As a first step, we compared the absorption spectra of the blood components oxyhemoglobin (HbO_2) and deoxyhemoglobin (Hb) [32, 33] with the absorption of **Re(NN3-OK)**, Figure 4A shows their molar extinction coefficients. It is clearly visible that the absorption of the complex strongly overlaps with the absorption

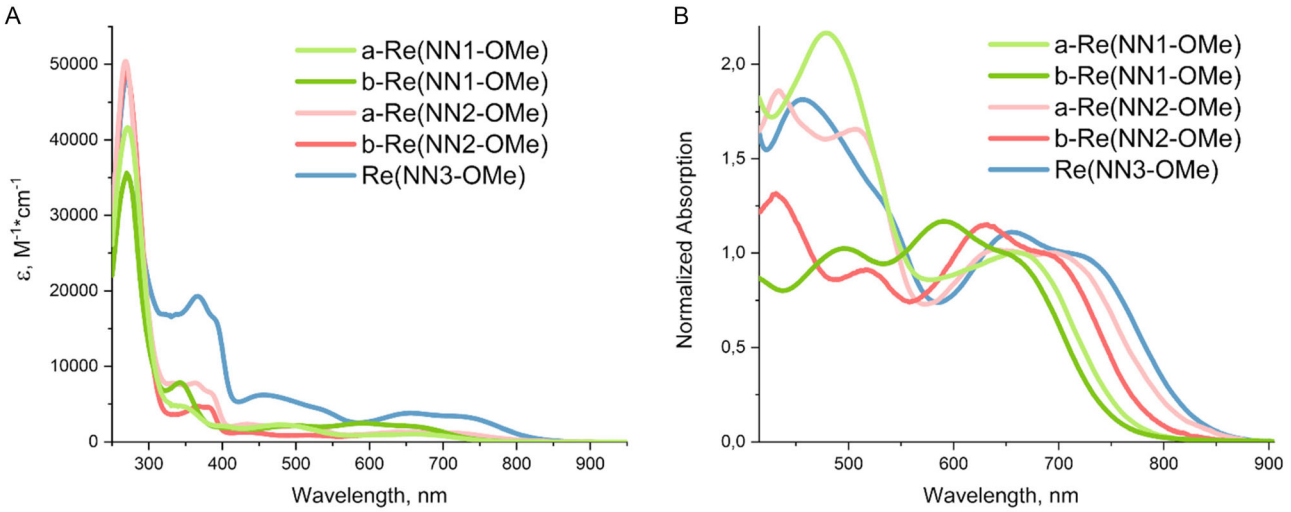

FIGURE 2 | (A) Absorption spectra of complexes **Re(NN#-OMe)**, methanol, 298K. (B) Fragment of absorption spectra of complexes **Re(NN#-OMe)** normalized at the lowest energy bands.

TABLE 1 | Absorption spectra of rhenium complexes, room temperature.

Complex	λ_{abs}, nm (ε 10^{-2} [cm^{-1} M^{-1}])
	Re(NN#-OMe), methanol
a-Re(NN1-OMe)	271 (*416*), 340 (*48*), 400 (*21*), 481 (*23*), 614sh (*9.5*), **665 (*10*)**
b-Re(NN1-OMe)	271 (*353*), 343 (*78*), 404 (*19*), 493 (*21*), 590 (*24*), **655 (*20*)**
a-Re(NN2-OMe)	268 (*504*), 333 (*78*), 363 (*78*), 382 (*66*), 433 (*23*), 514 (*20.5*), 644 (*13*), **700 (*13*)**
b-Re(NN2-OMe)	268 (*504*), 366 (*47*), 382 (*46*), 433 (*13*), 514 (*9*), 630 (*11.5*), **685 (*9.5*)**
Re(NN3-OMe)	270 (*484*), 365 (*193*), 386 (*165*), 459 (*62*), 528 (*45*), 656 (*38*), **715 (*32*)**
	Re(NN#-OK), methanol
a-Re(NN1-OK)	277 (*481*), 333 (*194*), 400 (*79*), 438 (*71*), **591 (*43*)**
a-Re(NN1-OH)	279 (*467*), 304sh (*300*), 340 (*206*), 457 (*79*), 616 (*42*), **665sh (*31*)**
b-Re(NN1-OK)	270 (*450*), 299 (*243*), 330 (*206*), 440 (*57*), 460 (*57*), 560 (*56*), **627 (*43*)**
b-Re(NN1-OH)	270 (*450*), 300sh (*202*), 339 (*203*), 400sh (*56*), 482 (*56*), 587 (*57*), **655 (*44*)**
a/b-Re(NN2-OK)	265 (*501*), 359 (*112*), 376 (*99*), 414 (*32*), 495 (*26*), 610 (*22*), **665 (*20*)**
a/b-Re(NN2-OH)	268 (*480*), 332 (*141*), 364 (*161*), 378 (*150*), 427 (*45*), 510 (*35*), 631 (*32*), 698 (*28*), **700 (*33*)**
Re(NN3-OK)	267 (*488*), 307sh (*220*), 361 (*190*), 376 (*179*), 418 (*55*), 480 (*46*), 610 (*38*), **661 (*32*)**
Re(NN3-OH)	270 (*494*), 370 (*197*), 401 (*210*), 455 (*78*), 644 (*38*), **715 (*33*)**
Re(NN3-OK)[a]	268 (*488*), 310sh (*213*), 362 (*180*), 380 (*169*), 424 (*52*), 490 (*42*), 620 (*34*), **673 (*30*)**
Re(NN3-OH)[a]	270 (*491*), 370 (*193*), 405 (*221*), 450 (*84*), 640 (*38*), **710 (*29*)**

[a]Recorded in H_2O

of Hb, while in the case of HbO_2, there is a region of dominant absorption of **Re(NN3-OK)**. Given that in a living organism the amount of HbO_2 varies from about 70% for venous blood to about 95% for arterial blood, we concluded that the 660–750 nm range may be suitable for detecting the **Re(NN3-OK)** photoacoustic signal.

Subsequently, a phantom (Figure 5C) containing three tubes with different chromophores—whole oxygenated blood (tube 1), **Re(NN3-OK)** complex in saline (tube 2), and **Re(NN3-OK)** complex in the 1:2 mixture saline/blood (tube 3)—was imaged using a PAT (photoacoustic tomography (PAT)) system across the wavelength range of 660–950 nm to assess the possibility of differentiating the developed dye from the main tissue chromophore via the photoacoustic method. Figure 4B shows photoacoustic spectra recorded in the systems. As expected, photoacoustic spectra differ from optical absorption due to wavelength-dependent fluence and system response; nevertheless, the dye retains a distinct peak near **720 nm** that is preserved in blood, enabling spectral separation.

The results of multispectral photoacoustic data processing provide separate chromophore distributions, as shown in Figure 5A–C. The images in Figure 5A,B clearly show that the reconstructed spatial distributions of oxygenated blood (shown in red) and the

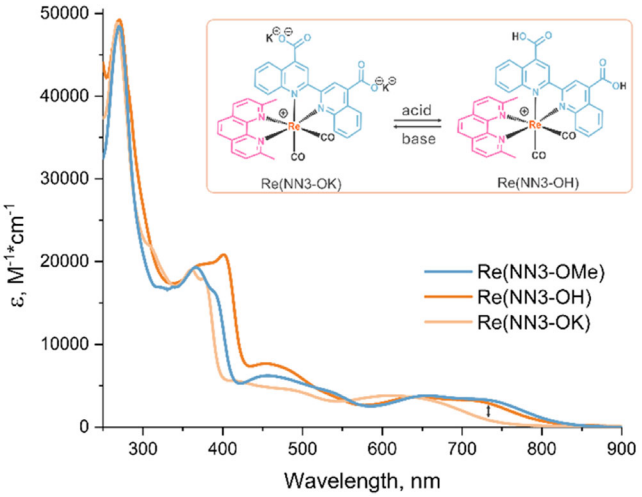

FIGURE 3 | Absorption spectra of complexes **Re(NN3-OMe)** in MeOH and under basic (in presence of K_2CO_3, **Re(NN3-OK)**) or acidic (in presence of CF_3COOH, **Re(NN3-OH)**) conditions of **Re(NN3-OK)** in aqueous media, 298 K.

Re(NN3-OK) complex (shown in yellow) correspond to the tubes containing each specific dye. Figure 5D shows a combined image of the spatial distributions of all chromophores considered and demonstrates the predominance of **Re(NN3-OK)** complex absorption over oxygenated blood in tube 3, which is due to the high concentration of the complex. These results demonstrate the possibility of reconstructing the distribution of the **Re(NN3-OK)** complex using photoacoustic multispectral imaging against the background of blood absorption.

These results demonstrate the potential applicability of the photoacoustic visualization method for tracking the distribution of this contrast agent in biological tissues and organs of small animals, as well as its accumulation in malignant neoplasms.

To ensure the biocompatibility of the **Re(NN3-OK)** probe, we conducted a cytotoxicity test to evaluate the viability of the CHO-K1 cell line using the MTT assay. After 24 h of incubation, no significant difference in proliferation capacity was observed compared to that in the control group (Figure 6). Additionally, no evident cytotoxicity was detected even at high concentrations of up to 1 mM. To further evaluate the long-term impact and broader applicability of the probe, we extended the cytotoxicity assessment to three cell lines (HeLa, HEK293, and CHO-K1) at a 96 h incubation period (Figure 6A). Concentrations below 50 μM showed no impact on cell proliferation in any of the tested cell lines. It is noteworthy that cells retained viability even at **Re(NN3-OK)** high concentrations (500 and 1000 μM) that exhibited antiproliferative effects, indicating that the compound inhibits proliferation without inducing acute cytotoxicity. Additionally, we evaluated the phototoxic potential of **Re(NN3-OK)** under laser irradiation conditions relevant to photoacoustic imaging applications. Cells were incubated with the **Re(NN3-OK)** probe (1, 10, and 100 μM) for 48 h, followed by irradiation with a 661 nm laser at 50 mW/cm^2 for 10 min. No phototoxicity was observed under these conditions, which employed continuous laser irradiation at higher power density than typical pulsed illumination in photoacoustic imaging protocols (Figure 6B). These results demonstrate the low cytotoxicity and high photostability of the **Re(NN3-OK)** probe, confirming its suitability for bioimaging in living systems.

To preliminarily evaluate the efficacy of the synthesized complex for in vivo OA signal generation relative to established contrast agents, we calculated the absorption coefficient at the maximum permissible concentration, α_{lim}. The maximum nontoxic concentration, N_{lim}, for ICG and gold nanorods was estimated from published MTT assay data after 24 h incubation period, and their literature extinction coefficients, ε_0, within the 700–900 nm tissue transparency window were used. The corresponding data for the **Re(NN3-OK)** complex were obtained from the results presented in this work.

As shown in Table 2, ICG exhibits a fivefold higher α_{lim} value compared to the synthesized **Re(NN3-OK)** complex. However, both ICG and **Re(NN3-OK)** demonstrate significantly higher α_{lim} values than gold nanorods. It should also be mentioned that ICG is well known for its phototoxicity, which is actively used in photodynamic therapy but may be undesirable in photoacoustic experiments [34, 38]. ICG aggregation also gives variations (often unpredictable) in the absorption spectrum, which results in

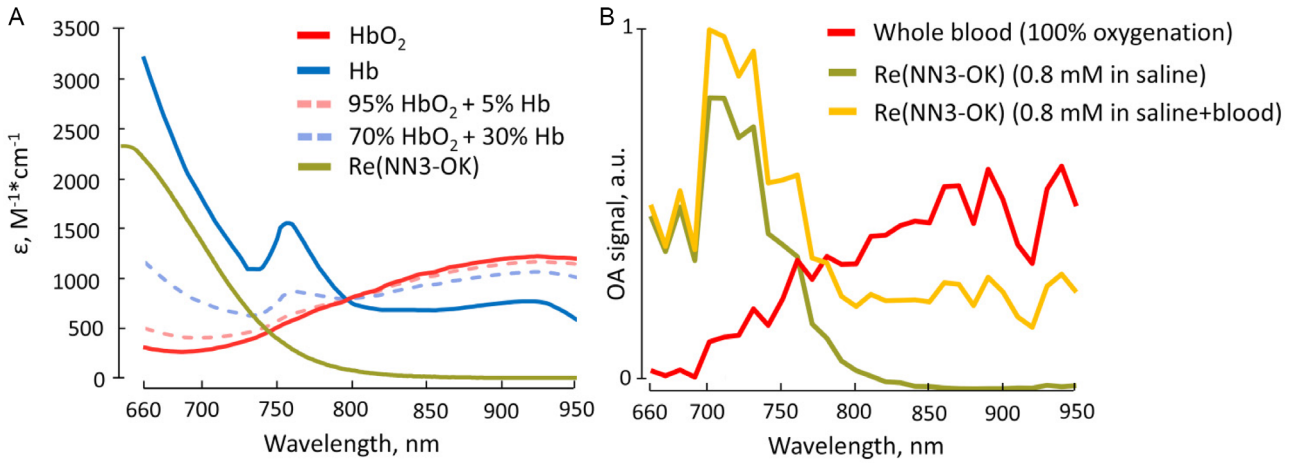

FIGURE 4 | (A) Reference molar extinction coefficients for HbO_2/Hb, their mixtures and molar extinction coefficients for **Re(NN3-OK)** complex in saline. (B) Photoacoustic spectra of oxygenated whole blood, 0.8 mM concentration of **Re(NN3-OK)** in saline, and 0.8 mM concentration of **Re(NN3-OK)**) in the mixture saline/blood (in 1:2 ratio).

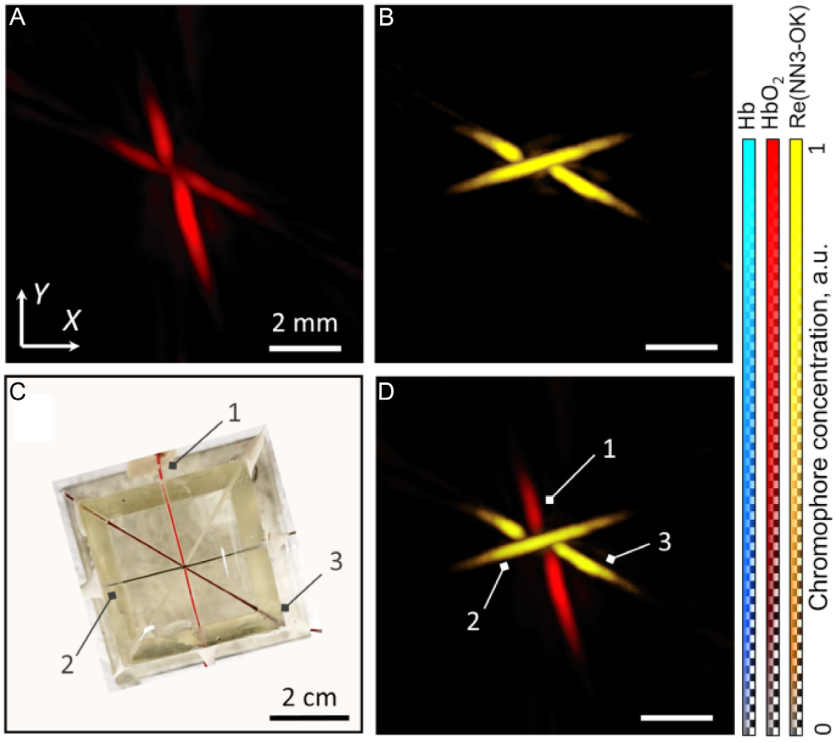

FIGURE 5 | Spatial distribution of different chromophores in the tubes of a phantom (C) reconstructed from multispectral photoacoustic imaging data: (A) Spatial distribution of HbO_2. (B) Spatial distribution of the **Re(NN3-OK)** complex. (D) Merged image of reconstructed chromophore distribution.

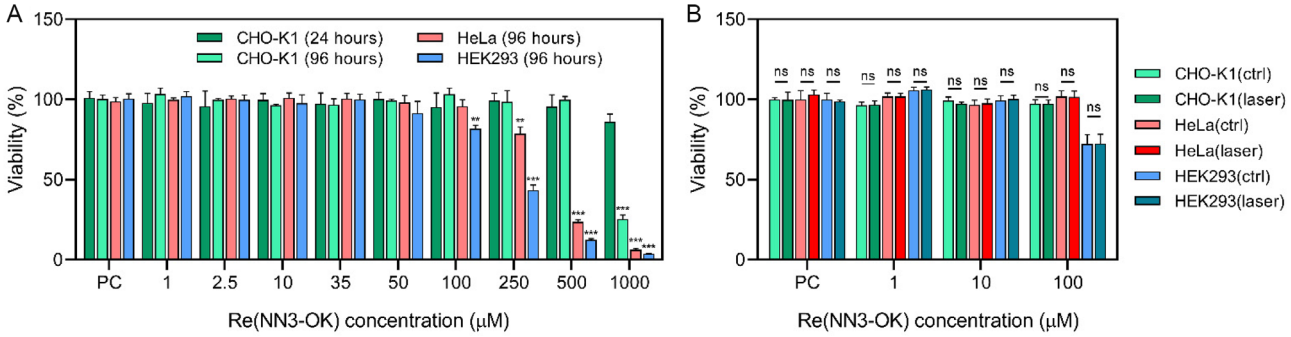

FIGURE 6 | Cytotoxicity and phototoxicity assessment of **Re(NN3-OK)** in HeLa, HEK293, and CHO-K1 cell lines. (A) Long-term cytotoxicity evaluation: cell viability after 24- or 96 h incubation with **Re(NN3-OK)** at different concentrations. (B) Phototoxicity assessment: cell viability following 48 h incubation with **Re(NN3-OK)** (1, 10, and 100 μM) and subsequent laser irradiation (661 nm, 50 mW/cm^2, 10 min). Cell viability of control cells (PC) was taken for 100%. The data are shown as mean ± SD of four replicates.

TABLE 2 | Comparison of contrast agent properties.

Contrast agent	N_{lim}, M	ε_0, M^{-1} cm^{-1}	α_{lim}, cm^{-1}	Wavelegth, nm	Ref.
ICG	5×10^{-5}	2×10^5	10	800	[34, 35]
Gold nanorods	6×10^{-11}	2×10^8	0.012	780	[36, 37]
Re(NN3-OK)	10^{-3}	2×10^3	2	700	Current Study

incorrect estimation of the contrast content in tissues/vessels recorded using PA measurements. In addition, the low photostability of ICG requires additional tools to improve its applicability [39, 40]. In contrast, **Re(NN3-OK)** shows high photostability and no phototoxicity, which make it a great candidate for further in vivo experiments. Nevertheless, it is important to note that other

critical factors—such as systemic toxicity, in vivo accumulation and elimination dynamics, and potential for functionalization or vectorization—are crucial for practical application and will be investigated in future in vivo studies.

3 | Conclusion

In summary, a new family of bis-diimine rhenium(I) complexes based on the ligands NN1-OMe – NN3-OMe containing quinoline moiety with an electron-withdrawing ester group have been successfully synthesized and characterized. The asymmetric structure of ligands NN1 and NN2 resulted in formation of two structural isomers named "a" and "b" with different types of coordination of the methylquinoline-4-carboxylate fragment. The presence of intramolecular $\pi\cdots\pi$ interaction between the aromatic systems of coordinated diimine ligands was revealed, which probably is one of the driving forces in formation of the target compound and determines the ratio of the "a" and "b" isomers. The **Re(NN#-OMe)** complexes absorb in almost the whole visible region of the spectrum. The expansion of aromatic system of the coordinated diimine and insertion of the electron-withdrawing substituents shift the low-energy absorption band of the ^{1}MLCT origin to the NIR region with its tail extending down to 850 nm (for **Re(NN3-OMe)**). Hydrolysis of the ester groups of the diimine ligands promoted the increase in hydrophilicity of the target compounds to give the best solubility in water in the case of **Re(NN3-OK)** containing two –COOK groups. Considering its highest absorption in the NIR region, **Re(NN3-OK)** was chosen as the most promising candidate for PAI. The results of phantom studies demonstrated clear separation of a Re complex signal on the background of pure blood absorption using multispectral PAT imaging. MTT tests showed that **Re(NN3-OK)** is not cytotoxic towards CHO-K1 cells if incubated for 24 h up to the concentrations of 1 mM. The obtained results allow concluding that the synthesized complexes may serve as a promising platform for preparation of rhenium chromophores suitable for effective PAI in the NIR range, including in vivo experiments. Estimation of the effect of substituents in the diimine ligands showed that insertion of electron withdrawing functions may shift the complex pKa to physiological interval, which open the way to practical application of the probe as a pH sensor in biological systems. We are now working on the synthesis of the corresponding ligands.

4 | Experimental Section

4.1 | General Comments

[(Neocuproine)Re(CO)$_2$(NCMe)$_2$]OTf (Re(NCCH$_3$)$_2$) [26] and 2-(pyridin-2-yl)quinoline-4-carboxylic acid (NN1-OH) [41] were synthesized according to the literature protocols. The carboxyl groups of diimine ligands NN1-OH—NN3-OH were converted to esters (NN1-OMe—NN3-OMe) by an esterification reaction in methanol in the presence of sulfuric acid [42]. Other reagents and solvents were used as received. Solution ^{1}H, 1H–^{1}H COSY, ^{1}H–^{1}H NOESY NMR spectra were recorded on a Bruker Avance III 400 MHz spectrometer. Chemical shifts in the NMR spectra are assigned using solvent residual signals. IR spectra were recorded with a Shimadzu IRAffinity-1 FTIR spectrophotometer in pressed KBr pellets or utilizing an ATR accessory. Mass spectra were measured on a Bruker maXis II ESI-QTOF instrument in the ESI$^+$ mode. Electronic absorption spectra were recorded at room temperature using a Shimadzu UV-1800 UV/Visible Scanning Spectrophotometer.

4.2 | The Synthesis of (2,2′-biquinoline)-4-carboxylic acid NN2-OH

The ligand was prepared by the modified procedure for the synthesis of 2-(pyridin-2-yl)quinoline-4-carboxylic acid [41]. 2,3-indolinedione (1.8 g, 0.012 mol) was mixed with 1-(quinolin-2-yl)ethan-1-one (1.4 g, 0.012 mol) in 20 mL of ethanol and 2 g of NaOH dissolved in 10 mL of H_2O were added with stirring. The solution was refluxed continuously for 24 h. After cooling to room temperature, the reaction mixture was acidified with aqueous solution of hydrochloric acid to pH 6. The resulting greenish solid was filtered, washed with water followed by cold acetone, diethyl ether and air dried.

^{1}H NMR (400 MHz, DMSO-d_6, δ) 9.16 (s, 1H), 8.77 (d, J = 8.6 Hz, 1H), 8.67 (d, J = 8.5 Hz, 1H), 8.58 (d, J = 8.6 Hz, 1H), 8.26 (d, J = 8.4 Hz, 1H), 8.20 (d, J = 8.4 Hz, 1H), 8.06 (d, J = 8.0 Hz, 1H), 7.91 (d, J = 7.4 Hz, 1H), 7.84 (d, J = 7.4 Hz, 1H), 7.78 (d, J = 7.7 Hz, 1H), 7.68 (t, J = 7.4 Hz, 1H), 4.06 (s, 3H). ESI$^+$ MS (m/z): 315.1136 [M+H]$^+$ (calc. 315.1134).

4.3 | General Procedure for the synthesis of the complexes [(Neocuproine)Re(NN#-OMe)(CO)$_2$]OTf Re(NN1-OMe)—Re(NN3-OMe)

Re(NCCH$_3$)$_2$ (50 mg, 0.094 mmol) and the corresponding diimine ligand (0.102 mmol) were dissolved in 1,2-dichlorobenzene (ca. 2 mL), the resulting suspension was purged with inert gas for 15 min and refluxed for 3 h under inert atmosphere. Then, the resulting solution was cooled to room temperature. For reaction with NN1, dark crystalline material, defined as **a-Re(NN1-OMe)**, was obtained, washed with diethyl ether and dried in vacuo. "b" isomer of **Re(NN1-OMe)** as well as complexes **a-Re(NN2-OMe)**, **a-Re(NN2-OMe)** and **Re(NN3-OMe)** were isolated from the corresponding reaction mixtures in 1,2-dichlorobenzene solution and purified by column chromatography (Silica gel 70–230 mesh, 1.5 × 20 cm, eluent dichloromethane → acetone → methanol). Then the products were recrystallized by the gas-phase diffusion of diethyl ether into acetone solution of **[(Neocuproine)Re(NN# - OMe)(CO)$_2$]OTf** at +5°C to give the black crystalline material.

a-Re(NN1-OMe). 40 mg, 70%. $C_{32}H_{24}N_4O_4Re$, $P2_1/n$, a = 12.01680(10), b = 18.6253(2), c = 14.67040(10) Å; β = 112.2770(10) °; V = 3038.40(5) Å^3, Z = 4, R_1 = 0.0272, CCDC 2 482 732. ^{1}H NMR (400 MHz, acetone-d_6, δ) 9.84 (d, J = 5.7 Hz, 1H), 8.86 (d, J = 8.2 Hz, 1H), 8.66 (s, 1H), 8.53 (d, J = 8.3 Hz, 1H), 8.42 (td, J = 7.9, 1.5 Hz, 1H), 8.36 (dd, J = 8.6, 1.0 Hz, 1H), 8.31 (d, J = 8.3 Hz, 1H), 8.24 (d, J = 8.3 Hz, 1H), 7.92 (ddd, J = 7.7, 5.8, 1.2 Hz, 1H), 7.72 (d, J = 8.7 Hz, 1H), 7.66 (d, J = 8.7 Hz, 1H), 7.60 (d, J = 8.4 Hz, 1H), 7.51 (ddd, J = 8.4, 7.0, 1.0 Hz, 1H), 7.25 (ddd, J = 8.6, 6.9, 1.2 Hz, 1H), 6.83 (d, J = 8.6 Hz, 1H), 4.01 (s, 3H), 3.62 (s, 3H). IR (KBr pellet, ν(C≡O), cm^{-1}): 1918s, 1845s. ESI$^+$ MS (m/z): 715.1366 [M]$^+$ (calc. 715.1356), 701.1206 [(M−CH$_3$)+H]$^+$ (calc. 701.1201).

b-Re(NN1-OMe). 12 mg, 21%. $C_{32}H_{24}N_4O_4Re$, *P−1*, $a = 12.4203(7)$, $b = 12.5329(6)$, $c = 12.6368(3)$ Å; $\alpha = 78.062(3)$, $\beta = 69.286(4)$, $\gamma = 85.245(4)$ °; $V = 1800.02(15)$ Å^3, $Z = 2$, $R_1 = 0.1264$, CCDC 2 482 733. ^{1}H NMR (400 MHz, acetone-d_6, δ) 9.54 (d, $J = 9.0$ Hz, 1H), 8.97–8.94 (m, 2H), 8.79 (d, $J = 8.4$ Hz, 1H), 8.72 (d, $J = 8.1$ Hz, 1H), 8.47 (d, $J = 8.4$ Hz, 1H), 8.35–8.26 (m, 2H), 8.23 (d, $J = 8.7$ Hz, 1H), 8.13–7.98 (m, 3H), 7.64 (d, $J = 8.4$ Hz, 1H), 7.20 (t, $J = 6.6$ Hz, 1H), 6.92 (d, $J = 5.6$ Hz, 1H), 4.15 (s, 3H), 3.59 (s, 3H), 1.75 (s, 3H). IR (KBr pellet, ν(C≡O), cm^{-1}): 1915s, 1845s. ESI$^+$ MS (*m*/*z*): 715.1366 [M]$^+$ (calc. 715.1356), 701.1206 [(M−CH$_3$)+H]$^+$ (calc. 701.1201).

a-Re(NN2-OMe). 29 mg, 42%. ^{1}H NMR (400 MHz, acetone-d_6, δ) 9.42 (d, $J = 8.8$ Hz, 1H), 8.95 (d, $J = 8.7$ Hz, 1H), 8.78 (d, $J = 8.8$ Hz, 1H),8.60 (s, 1H), 8.44 (d, $J = 8.3$ Hz, 1H), 8.42–8.35 (m, 3H), 8.30 (dd, $J = 8.5$, 0.8 Hz, 1H), 8.21 (d, $J = 8.3$ Hz, 1H), 8.06 (t, $J = 7.3$ Hz, 1H), 7.72–7.63 (m, Hz, 3H), 7.54 (ddd, $J = 8.5$, 6.9, 1.2 Hz, 1H), 7.37 (ddd, $J = 8.5$, 6.9, 1.5 Hz, 1H), 7.98 (d, $J = 8.7$ Hz, 1H), 4.04 (s, 3H), 3.75 (s, 3H), 1.68 (s, 3H). IR (KBr pellet, ν(C≡O), cm^{-1}): 1921s, 1852s. ESI$^+$ MS (*m*/*z*): 765.1493 [M]$^+$, (calc. 765.1513).

b-Re(NN2-OMe). 22 mg, 32%. ^{1}H NMR (400 MHz, acetone-d_6, δ) 9.52 (d, $J = 8.2$ Hz, 1H), 9.02 (d, $J = 1.6$ Hz, 1H), 8.97 (s, 1H), 8.47 (d, $J = 8.3$ Hz, 1H), 8.44–8.32 (m, 4H), 8.23 (d, $J = 8.3$ Hz, 1H), 8.12 (ddd, $J = 8.3$, 6.9, 1.1 Hz, 1H), 7.77 (d, $J = 8.1$ Hz, 1H), 7.73–7.66 (m, 2H), 7.64 (d, $J = 8.4$ Hz, 1H), 7.49 (t, $J = 8.4$ Hz, 1H), 7.33 (t, $J = 7.2$ Hz, 1H), 6.85 (d, $J = 8.1$ Hz, 1H), 4.17 (s, 3H), 3.77 (s, 3H), 1.72 (s, 3H). IR (KBr pellet, ν(C≡O), cm^{-1}): 1920s, 1851s. ESI$^+$ MS (*m*/*z*): 765.1493 [M]$^+$, (calc. 765.1513).

Re(NN3-OMe). 55 mg, 75%. ^{1}H NMR (400 MHz, acetone-d_6, δ) 9.49 (d, $J = 8.8$ Hz, 1H), 9.04–8.99 (m, 2H), 8.66 (s, 1H), 8.47 (d, $J = 8.3$ Hz, 1H), 8.42–8.36 (m, 2H), 8.30 (d, $J = 8.2$ Hz, 1H), 8.24 (d, $J = 8.3$ Hz, 1H), 8.14 (t, $J = 7.6$ Hz, 1H), 7.72–7.62 (m, 3H), 7.57 (t, $J = 7.8$ Hz, 1H), 7.37 (t, $J = 7.4$ Hz, 1H), 6.92 (d, $J = 8.7$ Hz, 1H), 4.17 (s, 3H), 4.04 (s, 3H), 3.77 (s, 3H), 1.72 (s, 3H). IR (KBr pellet, ν(C≡O), cm^{-1}): 1925s, 1856s. ESI$^+$ MS (*m*/*z*): 823.1538 [M]$^+$ (calc. 823.1568), 659.1443 [(Re(neocup)$_2$]$^+$ (calc. 659.1459).

4.4 | General Procedure for the Alkaline Hydrolysis of Re(NN1-OMe)—Re(NN3-OMe) Re(NN1-OK)—Re(NN3-OK)

The corresponding complex (0.005 mmol) and K_2CO_3 (0.05 mmol) were dissolved in methanol (5 mL). The reaction mixture was heated at 40°C overnight. The resulting solution was cooled down to 4°C, filtered through Celite, and the solvent was removed under reduced pressure to give the dark brown or dark green solid (ca. 90%).

a-Re(NN1-OK). ^{1}H NMR (400 MHz, CD_3OD, δ) 9.74 (d, $J = 5.3$ Hz, 1H), 8.59 (d, $J = 8.2$ Hz, 1H), 8.33 (d, $J = 8.3$ Hz, 1H), 8.24 (td, $J = 8.0$, 1.5 Hz, 1H), 8.18–8.13 (m, 2H), 8.11 (dd, $J = 8.5$, 1.4 Hz, 1H), 8.07 (d, $J = 8.3$ Hz, 1H), 7.68 (ddd, $J = 7.3$, 5.7, 1.4 Hz, 1H), 7.58–7.52 (m, 2H), 7.46 (d, $J = 8.3$ Hz, 1H), 7.30 (ddd, $J = 8.3$, 6.9, 1.2 Hz, 1H), 7.01 (ddd, $J = 8.5$, 6.8, 1.5 Hz, 1H), 6.61 (d, $J = 8.7$ Hz, 1H), 3.54 (s, 3H), 1.91 (s, 3H). IR (ATR accessory, ν(C≡O), cm^{-1}): 1920s, 1851s. ESI$^+$ MS (*m*/*z*): 701.1188 [(M−K)+H]$^{\pm}$ (calc. 701.1201), 723.1051 [(M−K)+Na]$^+$ (calc. 723.1020), 739.0712 [M]$^+$ (calc. 739.0757).

b-Re(NN1-OK). ^{1}H NMR (400 MHz, CD_3OD, δ) 9.43 (d, $J = 8.9$ Hz, 1H), 8.63 (dd, $J = 8.4$, 1.1 Hz, 1H), 8.58 (d, $J = 8.3$ Hz, 1H), 8.42–8.38 (m, 2H), 8.28 (d, $J = 8.4$ Hz, 1H), 8.14–8. 09 (m, 2H), 8.07 (d, $J = 8.6$ Hz, 1H), 7.98–7.88 (m, 2H), 7.83 (t, $J = 8.0$, 1H), 7.52 (d, $J = 8.3$ Hz, 1H), 6.97 (t, $J = 6.9$ Hz, 1H), 6.67 (d, $J = 6.6$ Hz, 1H), 3.54 (s, 3H), 1.69 (s, 3H). IR (ATR accessory, ν(C≡O), cm^{-1}): 1915s, 1843s. ESI$^+$ MS (*m*/*z*): 701.1188 [(M−K)+H]$^{\pm}$ (calc. 701.1201), 723.1051 [(M−K)+Na]$^+$ (calc. 723.1020), 739.0712 [M]$^+$ (calc. 739.0757).

a/b-Re(NN2-OK). IR (ATR accessory, ν(C≡O), cm^{-1}): 1918s, 1849s. ESI$^+$ MS (*m*/*z*): 723.1388 [$C_{34}H_{24}N_4O_3Re$]$^+$ (calc. 723.1408), 751.1333 [(M−K)+H]$^{\pm}$ (calc. 751.1358), 767.1301 [(M−K)+NH$_4$]$^+$ (calc. 767.1545), 781.1684 [(M−K)+(CH$_3$)NH$_3$]$^+$ (calc. 781.1701).

Re(NN3-OK). ^{1}H NMR (400 MHz, acetone-d_6, δ) 9.49 (d, $J = 8.8$ Hz, 1H), 9.04–8.99 (m, 2H), 8.66 (s, 1H), 8.47 (d, $J = 8.3$ Hz, 1H), 8.42 – 8.36 (m, 2H), 8.30 (dm, $J = 8.2$ Hz, 1H), 8.24 (d, $J = 8.3$ Hz, 1H), 8.14 (tm, $J = 7.6$ Hz, 1H), 7.69 (d, $J = 5.6$ Hz, 2H), 7.65 (d, $J = 8.5$ Hz, 1H), 7.57 (tm, $J = 7.8$ Hz, 1H), 7.39–7.35 (m, 1H), 6.92 (d, $J = 8.7$ Hz, 1H), 4.17 (s, 3H), 4.04 (s, 3H), 3.77 (s, 3H), 1.72 (s, 3H). IR (ATR accessory, ν(C≡O), cm^{-1}): 1914s, 1838s. ESI$^+$ MS (*m*/*z*): 795.1275 [(M−2K) + 2H]$^+$ (calc. 795.1256).

4.5 | X-Ray Structure Determination

Single crystals of **a-Re(NN1-OMe)** and **b-Re(NN1-OMe)** were carefully selected using an optical microscope under polarized light. The selected crystals were immersed in a cryoprotectant and then mounted on Nylon loops. XRD data were collected at 100 K using a Rigaku XtaLAB Synergy S X-ray diffractometer, equipped with a Hybrid Pixel Array Detector and a monochromatic microfocus CuKα PhotonJet (λ = 1.54184 Å) source.

The unit-cell parameters were refined via least-squares techniques. The structures were solved with a dual-space algorithm (SHELXT) [43] and then refined with full-matrix least-squares methods (SHELXL) [44] implemented in the OLEX2 program package [45].

The final structural models included anisotropic displacement parameters and atomic coordinates for all non-hydrogen atoms. Hydrogen atoms were arranged at calculated positions and refined via "riding" model with C—H bond lengths ranging from 1.085 to 1.095 Å. The supplementary crystallographic data are available via Supplementary Information section and have been deposited with the Cambridge Crystallographic Data Centre (CCDC) and are available via www.ccdc.cam.ac.uk/structures/.

a-Re(NN1-OMe). C32H24N4O4Re, P-1, $a = 12.4203(7)$, $b = 12.5329(6)$, $c = 12.6368(3)$, $\alpha = 78.062(3)$, $\beta = 69.286(4)$, $\gamma = 85.245(4)$°; $V = 1800.02(15)$ Å^3, $Z = 2$, $R1 = 0.1264$, CCDC 2 482 732.

b-Re(NN1-OMe). C32H24N4O4Re, P2$_1$/n, $a = 12.01680(10)$, $b = 18.6253(2)$, $c = 14.67040(10)$, $\alpha = 90$, $\beta = 112.2770(10)$, $\gamma = 90$°; $V = 3038.40(5)$ Å^3, $Z = 4$, $R1 = 0.0272$, CCDC 2 482 733.

4.6 | Photophysical Measurements

The UV–vis absorption spectra of **Re(NN#-OMe)** and **Re(NN#-OK)** were measured on a Shimadzu UV-1800 spectrophotometer in a 1 cm quartz cuvette (methanol, ca. 10^{-5} M).

Citrate-Phosphate buffer (pH 2.6–7.5) was used to prepare solutions of **Re(NN3-OK)** with various pH, lower pH values (1.5, 0.5) were adjusted by the addition of HCl. Exact pH values were determined using a pH-meter ("Expert pH", Econic-Expert) with a laboratory combined pH electrode (ESK-10 601/7). The pKa of **Re(NN3-OK)** were calculated according to the according to the modified equation [46, 47]

$$\mathrm{pKa} = \mathrm{pH} - \log\frac{D_x - D_{\mathrm{OK}}}{D_{\mathrm{OH}} - D_x}$$

where D_x-optical density at a defined pH within the titration plot, D_{OH}-optical density of the acid form, D_{OK}-optical density of the base form. The linear fit of the pH dependence *vs* $\log[(D_x - D_{\mathrm{OH}})/(D_{\mathrm{OK}} - D_x)]$ makes possible pKa calculation [46, 47].

4.7 | Computational Details

The fully optimized structures of ground singlet S_0 states were obtained within the DFT for all complexes under consideration. The calculations were performed using the Gaussian16 program [48]. The Austin–Frisch–Petersson hybrid density functional with dispersion correction (APFD) [49] was chosen for the most accurate description of experimental trends. The Stuttgart–Dresden effective core pseudopotential and the corresponding basis set were used for all atoms [50]. The non-specific solvation effects of appropriate solvents were taken into account by the polarizable continuum model (PCM) [51].

The electronic absorption spectra were calculated using TDDFT method taking in account 100 excited states for all complexes. The convoluting of UV/vis spectra from calculated oscillator strengths were obtained using home-made software based on the method described in library [52] modified for Lorentzian broadening.

Two approaches were used to describe the displacement of the electron density during absorption transition and to determine their character. A qualitative picture was established by the construction of approximate electronic density difference, $\Delta\rho$, using natural transition orbitals (NTO) [53]

$$\Delta\rho(S_0 \rightarrow S1) = |\varphi(\mathrm{LUMO})|^2 - |\varphi(\mathrm{HOMO})|^2$$

here $\varphi(\mathrm{LUMO})$ and $\varphi(\mathrm{HOMO})$ are first NTO pair for $S_0 \rightarrow S_1$ transition.

A number of electrons transferred between parts of the complexes have been obtained by IFCT (Interfragment charge transfer) method [54]. The Multiwfn 3.8 program [54, 55] was used for NTO and IFCT analysis.

4.8 | Photostability

The photostability test was carried out using the UWave-2000 Multifunctional Microwave Chemistry Reaction Workstation. The crystalline material of **Re(NN3-OK)** was dissolved in methanol, the resulting solution was diluted to about 10^{-5} M and continuously irradiated by the ultraviolet light with UV power of 300 W and the dominant wavelength of 365 nm for 2 h. The photostability of **Re(NN3-OK)** was examined by monitoring the absorbance of its 2.5 mL methanol solution in a 10 mm quartz cuvettes after 10, 30, 60 and 120 min of the UV irradiation as well as by recording the ^{1}H NMR spectra in CD_3OD after 120 min of the UV irradiation (Figure S34).

4.9 | Photoacoustic Experiments

4.9.1 | Setup for Measuring the Photoacoustic Spectrum of a Dye

The photoacoustic spectrum of the **Re(NN3-OK)** complex was studied using a custom volumetric PAT system. The PAT system consisted of a wavelength-tunable (660–1300 nm) pulsed laser (Ekspla, Lithuania), a 256-channel /12 bit Legion analog-to-digital converter (Photosound, USA), a three-coordinate positioning system consisting of two horizontal LTS150/M (Thorlabs, SSHA) and one vertical MLJ150/M (Thorlabs, SSHA) tables, a computer, and a 256-element spherical focused ultrasound antenna based on 25 μm thick PVDF film. The focal length and aperture of the antenna were 40 mm and 55 mm, the diameter of each element was 3 mm. To irradiate the tissues and phantoms under study with laser radiation, a 2 m long fiber optic bundle (CeramOptec, Germany) was fixed in the center of the antenna. The numerical aperture of the fiber optic was 0.22, the diameter of the light-guiding part was 5 mm, and the maximum laser irradiance for all the laser pulses was kept below 20 mJ/cm^2. Signals from the antenna were fed to an analog-to-digital converter with a sampling frequency of 40 MHz and then recorded on a computer via an interface in the Matlab software environment. Visualization of objects was carried out through an immersion chamber fixed on the antenna and filled with distilled water.

4.9.2 | Phantom for Photoacoustic Measurements

The phantom (Figure 5C) consisted of three polyurethane tubes (Putnam Plastics, USA) with an inner diameter of 0.3 mm and an outer diameter of 0.6 mm, fixed in a water-filled plastic form. The samples filled into the tubes were **Re(NN3-OK)** complex in a saline solution with a concentration of 0.8 mM, **Re(NN3-OK)** complex in saline + blood (in 1:2 ratio) with a concentration of 0.8 mM, and purely oxygenated blood taken from a sacrificed experimental rat provided by Privolzhsky Research Medical University. Measurements were performed in the wavelength range from 660 to 950 nm, performing two passes (forward and reverse) with a step of 10 nm at a laser pulse frequency of 20 Hz. After that, the signal was averaged over the two passes.

4.9.3 | Processing of Photoacoustic Data

The data were recorded as three-dimensional matrices: 1st dimension–antenna element number, 2nd dimension–signal arrival time, 3rd dimension–wavelength. The signals were normalized by the average laser energy for each excitation wavelength. The averaged energy of laser pulses at each wavelength was estimated using a pyroelectric energy sensor ES120C (Thorlabs, USA). The back projection reconstruction algorithm was applied to all two-dimensional arrays (element number, time) included in the three-dimensional array [56]. In this way, four-dimensional photoacoustic data arrays were obtained, where the first three dimensions represent spatial coordinates in a volume of $10 \times 10 \times 10$ mm^3 with a grid size of 100 μm, and the fourth dimension is the wavelength in the range of 660–950 nm with a step of 10 nm. Spectra were determined from

averaged signals at each wavelength from the central volume of $3 \times 3 \times 3$ voxels inside the tubes.

To display the spatial distribution of chromophores in the tubes, a multispectral reconstruction algorithm based on solving a system of linear equations was also applied to the four-dimensional data arrays. Spectral unmixing used non-negative least squares with a basis of energy-normalized reference spectra of HbO_2 and Hb from [32] (Figure 4A) and **Re(NN3-OK)** measured on the same system (Figure 4B). No fluence correction algorithms was applied, since all the tubes were coplanar at similar depths, minimizing spectral coloring differences. Subsequent visualization of the obtained relative chromophores concentrations was then visualized using Avizo Software 2024.1 (Thermo Fisher Scientific, USA), where each chromophore was assigned its own translucent color scale.

4.9.4 | MTT Assay

The CHO-K1, HeLa and HEK293 cell lines were kindly provided by the Russian Cell Culture Collection (Institute of Cytology, Russia). The cells were cultured in DMEM medium (for HeLa and HEK293) or DMEM/F12 medium (for CHO-K1) (Biolot, Russia), supplemented with 10% FBS (Capricorn Scientific, Germany), 2 mM L-glutamine, and 0.05 mg/mL gentamicin (PanEco, Russia). The day before the MTT assay, cells were seeded at a concentration of 1×10^4 cells per well (or 2.5×10^3 cells per well for 96 h incubation) in 96-well flat-bottom plates (TPP, Switzerland). Cells were incubated overnight in a humidified incubator at 37°C with 5% CO_2. The next day, the **Re(NN3-OK)** was dissolved in growth medium at different concentrations and added to the wells, followed by 24 h or 96 h incubation. After incubation, the medium was replaced with 200 µL of fresh culture medium, and 10 µL of MTT solution (5 mg/mL, PanEko, Russia) was added to each well. The cells were incubated for an additional 2 h, after which the MTT solution was removed and replaced with 100 µL of DMSO (Helicon, Russia) to dissolve the formazan crystals. The absorbance was measured at 570 nm using a SPECTROstar Nano microplate reader (BMG LABTECH, Germany). Cell viability was calculated as the ratio of the sample's optical density to that of the control. Data are presented as the mean ± standard deviation from a four independent replicates.

For evaluation of the **Re(NN3-OK)** phototoxicity, cells were seeded overnight in 96-well plate and then incubated for 48 h in the full growth medium containing **Re(NN3-OK)** at concentrations of 100, 10, and 1 µM. After removing the supernatant, fresh growth medium was added into each well. Subsequently, the cells were irradiated with a 661 nm laser (Coherent CUBE 660-100C) at a power density of 50 mW/cm^2 for 10 min (laser power was verified using a PM100 power meter, Thorlabs), and then cultured for an additional 1 h. Cell viability was determined using the standard MTT assay as described above. This phototoxicity assessment protocol was adapted from [57].

Acknowledgments

Synthesis, characterization, and optical studies of the rhenium(I) complexes were funded by the Russian Science Foundation, grant no. 19-73-20055-П. The work was performed using the equipment of the Research Park of St. Petersburg State University: Centers for Magnetic Resonance, for Chemical Analysis and Materials Research, for X-ray Diffraction Studies, for Computing, Cryogenic department; in commemoration of the 300th anniversary of St. Petersburg State University's founding. Photoacoustic experiments were supported by the Russian Science Foundation, grant no. 25-15−00238. The authors thank Privolzhsky Research Medical University for providing blood samples.

Conflicts of Interest

The authors declare no conflicts of interest.

Data Availability Statement

The data that support the findings of this study are available from the corresponding author upon reasonable request.

References

1. A. Taruttis and V. Ntziachristos, "Advances in Real-Time Multispectral Optoacoustic Imaging and Its Applications," *Nature Photonics* 9 (2015): 219–227.

2. X. Yang, Z. Jiang, J. Dai, Q. Fu, and S. Pan, "Photoacoustic Contrast Agents: A Review Focusing on Image-Guided Therapy," *Nanoscale Horizons* 10 (2025): 1285–1306.

3. L. V. Wang and J. Yao, "A Practical Guide to Photoacoustic Tomography in the Life Sciences," *Nature Methods* 13 (2016): 627–638.

4. J. Weber, P. C. Beard, and S. E. Bohndiek, "Contrast Agents for Molecular Photoacoustic Imaging," *Nature Methods* 13 (2016): 639–650.

5. J. T. Alander, I. Kaartinen, A. Laakso, et al., "A Review of Indocyanine Green Fluorescent Imaging in Surgery," *International Journal of Biomedical Imaging* 2021 (2012): 940585.

6. Y. Zheng, M. Liu, and L. Jiang, "Progress of Photoacoustic Imaging Combined with Targeted Photoacoustic Contrast Agents in Tumor Molecular Imaging," *Frontiers in Chemistry* 10 (2022): 1077937.

7. P. K. Upputuri and M. Pramanik, "Recent Advances in Photoacoustic Contrast Agents for In Vivo Imaging," *Wiley Interdisciplinary Reviews. Nanomedicine and Nanobiotechnology* 12 (2020): e1618.

8. S. Jeong, S. W. Yoo, H. J. Kim, et al., "Recent Progress on Molecular Photoacoustic Imaging with Carbon-Based Nanocomposites," *Materials* 14 (2021): 5643.

9. Ł. Niżnik, M. Noga, D. Kobylarz, et al., "Gold Nanoparticles (AuNPs)—Toxicity Safety and Green Synthesis: A Critical Review," *International journal of molecular sciences* 25 (2024): 4057.

10. P. M. Neelamraju, K. Gundepudi, P. K. Sanki, et al., "Potential Applications for Photoacoustic Imaging Using Functional Nanoparticles: A Comprehensive Overview," *Heliyon* 10 (2024): e34654.

11. A. Steinbrueck and J. Karges, "Metal Complexes and Nanoparticles for Photoacoustic Imaging," *Chembiochem* 24 (2023): e202300079.

12. Y. Xu, C. Li, Z. Y. Yu, et al., "Encapsulated Fe(IV) Molecular Complex for Photoacoustic Imaging," *CC Chemistry* 6 (2024): 1184–1197.

13. Z. Zhao, C. B. Swartchick, and J. Chan, "Targeted Contrast Agents and Activatable Probes for Photoacoustic Imaging of Cancer," *Chemical Society Reviews* 51 (2022): 829–868.

14. J. Zheng, Q. Zeng, R. Zhang, D. Xing, and T. Zhang, "Dynamic-Reversible Photoacoustic Probe for Continuous Ratiometric Sensing and Imaging of Redox Status In Vivo," *Journal of the American Chemical Society* 141 (2019): 19226–19230.

15. C. M. Worsley, R. B. Veale, and E. S. Mayne, "The Acidic Tumour Microenvironment: Manipulating the Immune Response to Elicit Escape," *Human Immunology* 83 (2022): 399–408.

16. Z. Yang, B. Gu, C. Jiang, L. Zhang, Q. Liu, and S. Song, "A pH-Responsive Photoacoustic Imaging Probe for Tumor pH Imaging In

Vivo Based on Polyaniline–bovine Serum Albumin," *Nanomedicine* 33 (2021): 102356.

17. A. V. Paderina, K. S. Kisel, V. V. Porsev, et al., "Shift It to the Red: The Synthesis of Dicarbonyl Re(I) Complexes with Two Different Diimine Ligands and Near-Infrared Luminescence," *Inorganic Chemistry* 64, no. 41 (2025): 20605–20614.

18. J. Granifo, M. T. Garland, and R. Baggio, "Stereoisomers of Palladium(II) Complexes with the Dipyridyl Ligands 2,3-Di(2-Pyridyl)pyrazine (dpp), 2,3-Di(2-Pyridyl)quinoxaline (dpq) and 6,7-Dimethyl-2,3-Di(2-Pyridyl)quinoxaline (ddpq). Crystal Structure of $[Pd(dpq)_2](PF_6)_2$," *Inorganica Chimica Acta* 348 (2003): 263–270.

19. C. R. Martinez and B. L. Iverson, "Rethinking the Term "Pi-Stacking," *Chemical Science* 3 (2012): 2191–2201.

20. J. L. Smithback, J. B. Helms, E. Schutte, S. M. Woessner, and B. P. Sullivan, "Preparative Routes to Luminescent Mixed-Ligand Rhenium(I) Dicarbonyl Complexes," *Inorganic Chemistry* 45 (2006): 2163–2174.

21. K. Sogawa, K. Minoura, Y. In, T. Ishida, T. Taniguchi, and K. Tomoo, "CH–π Interaction in VQIVYK Sequence Elucidated by NMR Spectroscopy Is Essential for PHF Formation of Tau," *Peptide Science* 102 (2014): 288–295.

22. G. Platzer, M. Mayer, A. Beier, et al., "PI by NMR: Probing CH–π Interactions in Protein–Ligand Complexes by NMR Spectroscopy," *Angewandte Chemie, International Edition* 59 (2020): 14861–14868.

23. S. Vandenbussche, D. Díaz, M. C. Fernández-Alonso, et al., "Aromatic–Carbohydrate Interactions: An NMR and Computational Study of Model Systems," *Chemistry–A European Journal* 14 (2008): 7570–7578.

24. R. J. Abraham and M. Reid, "^{1}H Chemical Shifts in NMR. Part 18.1 Ring Currents and π-Electron Effects in Hetero-Aromatics," *Journal of the Chemical Society, Perkin Transactions* 2 (2002): 1081–1091.

25. Y. Jin, B. Ramadoss, S. Asako, and L. Ilies, "Noncovalent Interaction with a Spirobipyridine Ligand Enables Efficient Iridium-Catalyzed C–H Activation," *Nature Communications* 15 (2024): 2886.

26. J. R. Shakirova, S. Nayeri, S. Jamali, et al., "Targeted Synthesis of NIR Luminescent Rhenium Diimine *Cis*, *Trans*-$[Re(NN)(CO)_2(L)_2]^{n+}$ Complexes Containing N -Donor Axial Ligands: Photophysical, Electrochemical, and Theoretical Studies," *ChemPlusChem* 85 (2020): 2518–2527.

27. H. Atallah, C. M. Taliaferro, K. A. Wells, and F. N. Castellano, "Photophysics and Ultrafast Processes in Rhenium(I) Diimine Dicarbonyls," *Dalton Transactions* 49 (2020): 11565–11576.

28. Y. Hameed, P. Berro, B. Gabidullin, and D. Richeson, "An Integrated Re(I) Photocatalyst/Sensitizer that Activates the Formation of Formic Acid From Reduction of CO_2," *Chemical Communications* 55 (2019): 11041–11044.

29. D. Sorsche, M. A. L. Lima, N. Meitinger, et al., "Shifting the MLCT of d6 Metal Complexes to the Red and NIR," *Coordination Chemistry Reviews* 530 (2025): 216454.

30. J. R. Shakirova, V. A. Baigildin, A. I. Solomatina, et al., "Intracellular pH Sensor Based on Heteroleptic Bis-Cyclometalated Iridium(III) Complex Embedded into Block-Copolymer Nanospecies: Application in Phosphorescence Lifetime Imaging Microscopy," *Advanced Functional Materials* 33 (2023): 2212390.

31. K. S. Kisel, V. A. Baigildin, A. V. Mozzhukhina, et al., "Biocompatible Re-Containing Block Copolymers for Intracellular pH Mapping in the PLIM Mode," *Inorganic Chemistry* 63 (2024): 16348–16361.

32. S. Prahl, "*Optical Absorption of Hemoglobin*," accessed July 2025, https://Omlc.Org/Spectra/Hemoglobin/.

33. I. V. Turchin, "Methods of Biomedical Optical Imaging: From Subcellular Structures to Tissues and Organs," *Physics-Uspekhi* 59 (2016): 487-501, https://doi.org/10.3367/ufne.2015.12.037734.

34. A. R. Montazerabadi, A. Sazgarnia, M. H. Bahreyni-Toosi, A. Ahmadi, and A. Aledavood, "The Effects of Combined Treatment with Ionizing Radiation and Indocyanine Green-Mediated Photodynamic Therapy on Breast Cancer Cells," *Journal of Photochemistry and Photobiology. B, Biology* 109 (2012): 42–49.

35. E. D. Cosco, I. Lim, and E. M. Sletten, "Photophysical Properties of Indocyanine Green in the Shortwave Infrared Region," *ChemPhotoChem* 5 (2021): 727–734.

36. K. P. Steckiewicz, E. Barcinska, A. Malankowska, et al., "Impact of Gold Nanoparticles Shape on Their Cytotoxicity against Human Osteoblast and Osteosarcoma in In Vitro Model. Evaluation of the Safety of use and Anti-Cancer Potential," *Journal of Materials Science Materials in Medicine* 30 (2019): 22.

37. A. Taruttis, E. Herzog, D. Razansky, and V. Ntziachristos, "Real-Time Imaging of Cardiovascular Dynamics and Circulating Gold Nanorods with Multispectral Optoacoustic Tomography," *Optics Express* 18 (2010): 19592–19602.

38. J. Lim, Y. Yoo, and Y. Choi, "Indocyanine Green-Loaded Quenched Nanoliposomes as Activatable Theranostics for Cancer," *Molecules* 30 (2025): 1414.

39. M. Szpunar, D. Aebisher, and A. Wal, "Changes in Absorption Spectra of Indocyanine Green after Visible Light Exposure and Cold Dark Storage," *Spectrochimica Acta. Part A, Molecular and Biomolecular Spectroscopy* 336 (2025): 126048.

40. Y.-D. Lee, H. J. Shin, J. Yoo, et al., "Metal Complexation-Mediated Stable and Biocompatible Nanoformulation of Clinically Approved Near-Infrared Absorber for Improved Tumor Targeting and Photonic Theranostics," *Nano Convergence* 8 (2021): 36.

41. B. N. Mongal, A. Pal, T. K. Mandal, J. Datta, and S. Naskar, "Synthesis, Characterisation, Electrochemical Study and Photovoltaic Measurements of a New Terpyridine and Pyridine-Quinoline Based Mixed Chelate Ruthenium Dye," *Polyhedron* 102 (2015): 615–626.

42. Z. Hendi, D. O. Kozina, V. V. Porsev, K. S. Kisel, J. R. Shakirova, and S. P. Tunik, "Investigation of the N^C Ligand Effects on Emission Characteristics in a Series of Bis-Metalated $[Ir(N^C)_2(N^N)]^+$ Complexes," *Molecules* 28 (2023): 2740.

43. G. M. Sheldrick, "SHELXT – Integrated Space-Group and Crystal-Structure Determination," *Acta Crystallographica, Section A: Foundations of Crystallography* 71 (2015): 3–8.

44. G. M. Sheldrick, "Crystal Structure Refinement with SHELXL," *Acta Crystallographica. Section C, Structural Chemistry* 71 (2015): 3–8.

45. O. V. Dolomanov, L. J. Bourhis, R. J. Gildea, J. A. K. Howard, and H. Puschmann, "OLEX2: A Complete Structure Solution, Refinement and Analysis Program," *Journal of Applied Crystallography* 42 (2009): 339–341.

46. A. Lobnik, I. Oehme, I. Murkovic, and O. S. Wolfbeis, "PH Optical Sensors Based on Sol–gels: Chemical Doping versus Covalent Immobilization," *Analytica Chimica Acta* 367 (1998): 159–165.

47. X. Zhang, G.-J. Song, X.-J. Cao, et al., "A New Fluorescent pH Probe for Acidic Conditions," *RSC Advances* 5 (2015): 89827–89832.

48. M. J. Frisch, G. W. Trucks, H. B. Schlegel, et al., Gaussian 16, Revision C.01 (Gaussian, Inc, 2016).

49. A. Austin, G. A. Petersson, M. J. Frisch, F. J. Dobek, G. Scalmani, and K. Throssell, "A Density Functional with Spherical Atom Dispersion Terms," *Journal of Chemical Theory and Computation* 8 (2012): 4989–5007.

50. D. Andrae, U. Häußermann, M. Dolg, H. Stoll, and H. Preuß, "Energy-Adjusted Ab Initio Pseudopotentials for the Second and Third Row Transition Elements," *Theoretica Chimica Acta* 77 (1990): 123–141.

51. J. Tomasi, B. Mennucci, and R. Cammi, "Quantum Mechanical Continuum Solvation Models," *Chemical Reviews* 105 (2005): 2999–3094.

52. N. M. O'boyle, A. L. Tenderholt, and K. M. Langner, "Cclib: A Library for Package-Independent Computational Chemistry Algorithms," *Journal of Computational Chemistry* 29 (2008): 839–845.

53. R. L. Martin, "Natural Transition Orbitals," *The Journal of Chemical Physics* 118 (2003): 4775–4777.

54. T. Lu and F. Chen, "Multiwfn: A Multifunctional Wavefunction Analyzer," *Journal of Computational Chemistry* 33 (2012): 580–592.

55. T. Lu, "A Comprehensive Electron Wavefunction Analysis Toolbox for Chemists, Multiwfn," *The Journal of Chemical Physics* 161 (2024): 082503.

56. P. V. Subochev, X. L. Deán-Ben, Z. Chen, et al., "Ultrawideband High Density Polymer-based Spherical Array for Real-Time Functional Optoacoustic Micro-Angiography," *Light: Science & Applications* 14 (2025): 239.

57. Q. Yang, H. Jin, Y. Gao, J. Lin, H. Yang, and S. Yang, "Photostable Iridium(III)–Cyanine Complex Nanoparticles for Photoacoustic Imaging Guided Near-Infrared Photodynamic Therapy In Vivo," *ACS Applied Materials & Interfaces* 11 (2019): 15417–15425, https://doi.org/10.1021/acsami.9b04098.

Supporting Information

Additional supporting information can be found online in the Supporting Information section. **Supporting Fig. S1:** Schematic representation and molecular views of all the isomers in the solid state for **a-Re(NN1-OMe)** (A) and of **b-Re(NN1-OMe)** (B). The thermal ellipsoids are shown at the 50% (A) or 30% (B) probability level. Hydrogen atoms are omitted for clarity. Rhenium atoms are given in orange color, oxygen – red, nitrogen – blue, carbon – gray. **Supporting Fig. S2:** Fragments of **a-Re(NN1-OMe)** (A) and of **b-Re(NN1-OMe)** (B) molecular packing in crystal cells showing several short intermolecular contacts. **Supporting Fig. S3:** ^{1}H NMR spectrum of complex **a-Re(NN1-OMe)**, acetone- d_6, 298 K, 400 MHz. **Supporting Fig. S4:** (A) Fragment of ^{1}H NMR spectrum with proton assignment, (B) ^{1}H-^{1}H COSY and (C) ^{1}H-^{1}H NOESY NMR of complex **a-Re(NN1-OMe)**, acetone- d_6, 298K, 400 MHz. **Supporting Fig. S5:** ^{1}H NMR spectrum of complex **b-Re(NN1-OMe)**, acetone- d_6, 298K, 400 MHz. **Supporting Fig. S6:** (A) Fragment of ^{1}H NMR spectrum with proton assignment, (B) ^{1}H-^{1}H COSY and (C) ^{1}H-^{1}H NOESY NMR of complex **b-Re(NN1-OMe)**, acetone- d_6, 298K, 400 MHz. **Supporting Fig. S7:** ^{1}H NMR spectrum of complex **a-Re(NN2-OMe)**, acetone- d_6, 298K, 400 MHz. **Supporting Fig. S8:** (A) Fragment of ^{1}H NMR spectrum with proton assignment, (B) ^{1}H-^{1}H COSY and (C) ^{1}H-^{1}H NOESY NMR of complex **a-Re(NN2-OMe)**, acetone- d_6, 298K, 400 MHz. **Supporting Fig. S9:** ^{1}H NMR spectrum of complex **b-Re(NN2-OMe)**, acetone- d_6, 298K, 400 MHz. **Supporting Fig. S10:** (A) Fragment of ^{1}H NMR spectrum with proton assignment, (B) ^{1}H-^{1}H COSY and (C) ^{1}H-^{1}H NOESY NMR of complex **b-Re(NN2-OMe)**, acetone- d_6, 298K, 400 MHz. **Supporting Fig. S11:** ^{1}H NMR spectrum of complex **Re(NN3-OMe)**, acetone- d_6, 298K, 400 MHz. **Supporting Fig. S12:** (A) Fragment of ^{1}H NMR spectrum with proton assignment, (B) ^{1}H-^{1}H COSY and (C) ^{1}H-^{1}H NOESY NMR of complex **Re(NN3-OMe)**, acetone- d_6, 298K, 400 MHz. **Supporting Fig. S13:** ^{1}H NMR spectrum of complex **a-Re(NN1-OK)**, methanol-d_4, 298K, 400 MHz. **Supporting Fig. S14:** (A) Fragment of ^{1}H NMR spectrum with proton assignment, (B) ^{1}H-^{1}H COSY and (C) ^{1}H-^{1}H NOESY NMR of complex **a-Re(NN1-OK)**, methanol-d_4, 298K, 400 MHz. **Supporting Fig. S15:** ^{1}H NMR spectrum of complex **b-Re(NN1-OK)**, methanol-d_4, 298K, 400 MHz. **Supporting Fig. S16:** (A) Fragment of ^{1}H NMR spectrum with proton assignment, (B) ^{1}H-^{1}H COSY and (C) ^{1}H-^{1}H NOESY NMR of complex **b-Re(NN1-OK)**, methanol-d4, 298K, 400 MHz. **Supporting Fig. S17:** ^{1}H NMR spectrum of complex **Re(NN3-OK)**, methanol-d_4, 298K, 400 MHz. **Supporting Fig. S18:** (A) Fragment of ^{1}H NMR spectrum with proton assignment, (B) ^{1}H-^{1}H COSY and (C) ^{1}H-^{1}H NOESY NMR of complex **Re(NN3-OK)**, methanol-d_4, 298K, 400 MHz. **Supporting Fig. S19:** ^{1}H NMR spectrum of mixture **a/b-Re(NN2-OK)**, acetone- d_6, 298K, 400 MHz. **Supporting Fig. S20:** ESI$^+$ HRMS of **Re(NN1-OMe) — Re(NN3-OMe)** (top) and **Re(NN1-OK) — Re(NN3-OK)** (bottom). **Supporting Fig. S21:** IR spectra of **Re(NN1-OMe) — Re(NN3-OMe)** in the carbonyl region (KBr pellet). **Supporting Fig. S22:** spectra of **Re(NN1-OK) — Re(NN3-OK)** in the carbonyl region (ATR accessory). **Supporting Fig. S23:** Electronic absorption spectra of the acid (in presence of CF_3COOH) and base (in presence of DBU) forms of complexes: A. **a-Re(NN1-OH/OK)**, B. **b-Re(NN1-OH/OK)**, C. **a/b-Re(NN2-OH/OK)**, D. **Re(NN3-OH/OK)** in MeOH, 293K. **Supporting Fig. S24:** A: Dependence of **Re(NN3-OK)** absorption spectra on pH, 293K, aqueous buffers. B: Dependence of **Re(NN3-OK)** absorbance at 730 nm on pH, 293K. C. pH vs. $\log[(D_x\text{-}D_{OH})/(D_{OK}\text{-}D_x)]$ plot for **Re(NN3-OK)** and it's linear fit. **Supporting Fig. S25:** The experimental (solid lines) and calculated (dotted lines) absorption spectra of **a-Re(NN1-R)**: base form – black lines, acid form – red lines. **Supporting Fig. S26:** NTOs demonstrating the decrease (violet) and increase (terracota) of electrondensity for $S_0 \rightarrow S_1$ electronic absorption transitions of **a-Re(NN1-R)** in MeOH. **Supporting Fig. S27:** The experimental (solid lines) and calculated (dotted lines) absorption spectra of **b-Re(NN1-R)**: base form – black lines, acid form – red lines. **Supporting Fig. S28:** NTOs demonstrating the decrease (violet) and increase (terracota) of electrondensity for $S_0 \rightarrow S_1$ electronic absorption transitions of **b-Re(NN1-R)**. **Supporting Fig. S29:** The experimental (solid lines) and calculated (dotted lines) absorption spectra of **a/b-Re(NN2-R)**: base form – black and violet lines, acid form – red and orange lines. **Supporting Fig. S30:** NTOs demonstrating the decrease (violet) and increase (terracota) of electrondensity for $S_0 \rightarrow S_1$ electronic absorption transitions of **a-Re(NN2-R)** in MeOH. **Supporting Fig. S31:** NTOs demonstrating the decrease (violet) and increase (terracota) of electron density for $S_0 \rightarrow S_1$ electronic absorption transitions of **b-Re(NN2-R)** in MeOH. **Supporting Fig. S32:** The experimental (solid lines) and calculated (dotted lines) absorption spectra of **Re(NN3-R)**: base form – black lines, acid form – red lines. **Supporting Fig. S33:** NTOs demonstrating the decrease (violet) and increase (terracota) of electrondensity for $S_0 \rightarrow S_1$ electronic absorption transitions of **Re(NN3-R)** in H_2O. **Supporting Fig. S34: A**: Normalized absorption spectra of the methanol solution of **Re(NN3-OK)** before and after irradiation by the ultraviolet light with the dominant wavelength of 365nm and UV power of 300W. **B**: ^{1}H NMR spectra of **Re(NN3-OK)** (aromatic region) before (green) and after (pink) irradiation by the ultraviolet light with the dominant wavelength of 365nm and UV power of 300W, MeOD, 298K, 400 MHz. **Supporting Table S1:** Crystal data and structure refinement for **a-Re(NN1-OMe)** and **b-Re(NN1-OMe)**. **Supporting Table S2:** Major structural parameters of **a-Re(NN1-OMe)** and **b-Re(NN1-OMe)**. **Supporting Table S3:** Calculated absorption maxima for S_0-S_1 transitions for complexes **Re(NN1-R)−Re(NN3-R)**. **Supporting Table S4:** IFCT of $S_0 \rightarrow S_1$ electronic excitation in **a-Re(NN1-R)** in MeOH. **Supporting Table S5:** IFCT of $S_0 \rightarrow S_1$ electronic excitation in **b-Re(NN1-R)** in MeOH. **Supporting Table S6:** IFCT of $S_0 \rightarrow S_1$ electronic excitation in **a-Re(NN2-R)** in MeOH. **Supporting Table S7:** IFCT of $S_0 \rightarrow S_1$ electronic excitation in **b-Re(NN2-R)** in MeOH. **Supporting Table S8:** IFCT of $S_0 \rightarrow S_1$ electronic excitation in **Re(NN3-R)** in H_2O.